Research Article
doi.org/10.1002/slct.202501255

Chemistry Europe
European Chemical Societies Publishing

www.chemistryselect.org

Sol–Gel Synthesis of Mn_2O_3–WO_3 Nanocomposites for the Photocatalytic Degradation of Mixed Parabens

Eric M. Ngigi,*[a] Philiswa N. Nomngongo,[b] Alex M. Muthengi,[c] Joseph K. Mworia,[d] and Jane C. Ngila[b]

Pharmaceutical and personal care products (PPCPs) are emerging environmental contaminants because of their potential and persistent adverse impacts on human and animal health. This study aims to synthesize WO_3 and Mn_2O_3–WO_3 nanocomposites using the sol–gel method as potential degraders of mixed parabens. When exposed to visible light, these nanocomposites show enhanced photocatalytic efficiency for the removal of mixed parabens, such as methylparaben and propylparaben. Transmission electron microscopy (TEM) analysis of the nanocomposites revealed that the ovoid-like WO_3 and rod-like Mn_2O_3 structures are responsible for increased photocatalytic activity. Decarboxylation, dealkylation, hydroxyl radicals, and hydroxylation played a significant role in the photodegradation process. The results revealed that the rates of removal of methylparaben and propylparaben mediated by Mn_2O_3–WO_3 nanocomposite photocatalyst under visible light amounted to 72% and 85%, respectively. The findings of the study demonstrated the potential of Mn_2O_3–WO_3 nanocomposites as an alternative technique for removing organic contaminants from water; hence, offering a practical remedy for water contamination caused by parabens and other similar pollutants.

1. Introduction

Environmental contaminants have recently attracted a lot of attention due to the risks they pose to living things and the environment.[1] They are frequently found in trace levels and have a variety of structural traits and behaviors, and they result in a range of impacts and modes of action in both the environment and the human body. Public health and environmental integrity are seriously and increasingly threatened by their presence.[2] Most of these substances continue to be poorly understood and unregulated, hence entering the ecosystems, food chains, and water supplies. Adjustments to hormonal public health systems must be dealt with since new challenges result in widespread contamination, which poses possible health risks.[3]

Some of these contaminants are parabens, which are esters of ρ-hydroxybenzoic acid that have been used extensively for almost a century due to their superior antimicrobial qualities.[4] Among the consumer products that contain these substances are, but are not limited to, foodstuffs, drinks, medications, and personal care.[5] Due to their widespread use, they are frequently found in aquatic environments at concentrations as low as µg/L.[6] Several studies have documented these paraben levels in various regions. According to Peng et al.,[7] methylparaben and ethylparaben concentrations in Chinese rivers were found to be 3142 and 1060 ng/L, respectively, while Indian rivers have recorded higher ethylparaben levels[8] and European rivers have reported methylparaben concentrations up to 400 ng/L.[9] Breast cancer poses high negative health effects associated with prolonged exposure to parabens due to their widespread presence in aquatic systems.[10–12] Due to the hazards posed to both environmental and human health, an effective technique is needed to eliminate parabens. Therefore, a viable strategy is the application of semiconductor-based photocatalysts like tungsten oxide (WO_3), which has shown promise in the degradation of contaminants when exposed to visible light. With a moderate bandgap (E_g = 2.4–2.7 eV), WO_3 is an n-type semiconductor that is appealing for photocatalytic applications. A high electron-hole recombination rate limits its usefulness and lowers its efficiency. To overcome this limitation, scientists have investigated coupling WO_3 with other semiconductors to suppress charge carrier recombination. Such hybrid systems have shown promise in various applications, including the photocatalytic degradation of organic pollutants,[13–16] gas sensing,[17] and photoelectrochemistry.[18,19]

Recently, attention has been directed toward the development of inexpensive transition metal oxides, such as manganese oxides, which are abundant in nature and provide several benefits for both industrial and environmental applications due to their low cost. Manganese oxide nanoparticles have gained considerable interest because of their adaptability in fields such as biomedical research, photocatalysis, and supercapacitor technology.[20–23] These nanoparticles make them valuable

[a] E. M. Ngigi
Department of Chemistry, Multimedia University of Kenya, P.O. Box 15653-00503, Nairobi, Kenya
E-mail: eric.mwangi@mmu.ac.ke

[b] P. N. Nomngongo, J. C. Ngila
Department of Chemical Sciences, University of Johannesburg, P.O. Box 17011, Doornfontein Campus, Johannesburg 2028, South Africa

[c] A. M. Muthengi
Department of Basic Sciences, Tharaka University, P.O. Box 193–60215, Marimanti, Kenya

[d] J. K. Mworia
Department of Physical Sciences, Meru University of Science and Technology, P.O. Box 972–60200, Meru, Kenya

due to their varied crystal structures, valence states, low cost, no toxicity, ease of synthesis, and natural abundance. Mn_2O_3 is one of the most promising manganese oxides because of its remarkable physical and chemical characteristics, high theoretical capacity, non-toxicity, and structural flexibility. Because of its low cost and practicality.[24] Mn_2O_3 has become a popular choice for applications such as catalysis,[25,26] biosensors,[27] batteries,[28] and supercapacitors.[29,30]

Shanmugapriya and Kanthavel[31] have previously reported the application of Mn_2O_3–WO_3 nanocomposites for dye removal, and the current study demonstrates the use of synthesized sol–gel Mn_2O_3–WO_3 nanomaterials for the effective removal of mixed parabens from aqueous solutions. This is an innovative method for the removal of environmental contaminants.

2. Experimental Section

2.1. Chemicals

Citric acid ($C_6H_8O_7$), manganese chloride ($MnCl_2{\cdot}4H_2O$), sodium tungstate (Na_2WO_4), propylparaben (propyl-4-hydroxybenzoate), and methylparaben (methyl-4-hydroxybenzoate) were obtained from Sigma–Aldrich, St. Louis, MI, USA, and hydrochloric acid (HCl, 32%), ammonia (25% v/v), and absolute ethanol (99.9%) were obtained from Minema, Johannesburg, South Africa. No purification was required for any of the acquired chemicals. Deionized water was used in all the experiments.

2.2. Material Synthesis

The WO_3 nanostructure was synthesized with modification using the sol–gel method.[32] Initially, 4 g of sodium tungstate was dissolved in a mixture of 50 mL of ethanol and deionized water (in a 2:1 ratio) under continuous stirring. Subsequently, 2 mL of HCl was added to the mixture and stirred for 3 h. After reaching room temperature, the solution was washed multiple times with distilled water and ethanol, followed by drying at 60 °C for 12 h.

A similar approach was employed to prepare the Mn_2O_3–WO_3 nanocomposite. Approximately 1 g of $MnCl_2$ was dissolved in 50 mL of methanol and stirred for 10 min. Then, 2.0 g of the as-prepared WO_3 was added to the solution and stirred for an additional 15 min. Ammonia was added dropwise, and the mixture was stirred for another 3 h. The solution was aged for 24 h, washed several times with distilled water and ethanol, and dried overnight at 60 °C. Finally, the powder was calcined at 500 °C for 2 h with a heating rate of 10 °C/min in a muffle furnace. The synthesis procedure for the Mn_2O_3–WO_3 nanocomposite is illustrated in Figure 1. The pristine Mn_2O_3 nanoparticles were synthesized following the same procedure without the addition of the as-prepared WO_3.

2.3. Characterizations

The crystal phases of the as-synthesized samples were analyzed by powder X-ray diffractometer (Philips X'Pert-PRO PANalytical, Amsterdam, the Netherlands). The morphologies and particle sizes were determined using a scanning electron microscope (Tescan Vega, Brno, Czechia). High-resolution transmission electron microscope (HRTEM) and selected area electron diffraction (SAED) images were obtained using a Jeol (JEM-2100, Kyoto, Japan) with an acceleration voltage of 200 kV. The surface area was evaluated using nitrogen absorption–desorption isotherms and adsorption data at −197 °C using the Brunauer–Emmett–Teller (BET) method (Micrometrics ASAP 2020, Norcross, GA, USA). Optical characterization of the samples was performed at room temperature using a UV–vis diffuse reflection spectrophotometer (UV-DRS, Shimadzu 2450, Kyoto, Japan) using $BaSO_4$ as a reference, and a photoluminescence spectrophotometer (Model: LS45) using a PerkinElmer, Inc. (Waltham, MA, USA).

2.4. Photocatalytic Experiment

The adsorption and photocatalytic degradation efficiency of mixed parabens in an aqueous solution at room temperature was evaluated using a 300 W Xenon lamp fitted with a UV cut-off filter to provide visible light ($\lambda > 420$ nm), effectively blocking wavelengths below 420 nm. Before light exposure, 30 mg of the photocatalyst was dispersed in 50 mL of a 10 ppm solution, sonicated for 10 min, and then magnetically stirred in the dark for 30 min to achieve adsorption–desorption equilibrium. During irradiation, approximately 3 mL of the solution was sampled at 15 min intervals, followed by centrifugation at 6000 rpm for 10 min to separate the photocatalysts. The following equation determines the degradation efficiency.

$$\text{DEGRADATION}\,(\%) = 1 - \frac{C_t}{C_o} \times 100$$

where C_o is the initial concentration of mixed parabens and C_t is the concentration at a given time interval.

2.5. Analytical Procedures

The propylparaben and methylparaben concentrations were determined using an inductively coupled plasma mass spectrometer–liquid chromatograph (ICP-MS-LC) equipped with an Agilent Zorbax Eclipse plus C18 column (3.5 µm × 150 mm × 4.6 mm) (Agilent, Newport, CA, USA). The column was maintained at 25 °C. Before injection, the samples were filtered through a 0.45 µm membrane filter. The injection volume was set at 5 µL and the gradient eluent (methanol/water) was pumped at a rate of 1.000 mL/min for 15 min. The detection was performed with a diode array detector at wavelengths of 250 and 260 nm.

3. Results and Discussion

3.1. Structure and Morphology of Mn_2O_3–WO_3 Nanocomposite

The crystal structure of the photocatalyst was characterized by powder X-ray diffraction (PXRD), as shown in Figure 2. The as-prepared WO_3 nanoflower exhibited a highly crystallized phase that can be indexed as belonging to the orthorhombic crystal system when compared with ICDD: 04-007-0880. The reflections at 2θ values of 19.61°, 21.97°, 24.22°, 28.61°, and 36.18° correspond to (101), (111), (020), (200), and (220). The pure Mn_2O_3 demonstrates distinct peaks at 2θ values of 23.13°, 32.95°, 38.24°, 55.19°, and 65.81°, corresponding to (211), (222), (400), (440), and (622), respectively, which align well with the cubic bixbyite Mn_2O_3 (ICDD: 00-041-1442).[33] The decoration of Mn_2O_3 nanoparticles

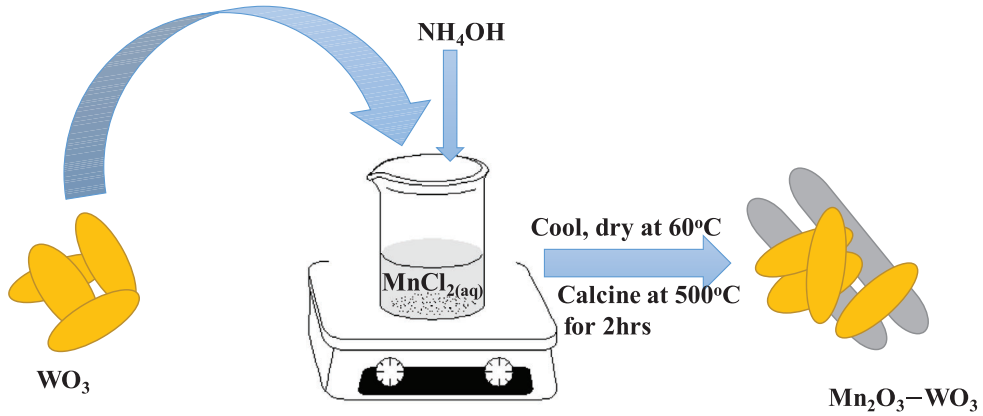

Figure 1. Illustration of the procedure for synthesizing the Mn_2O_3–WO_3 nanocomposite.

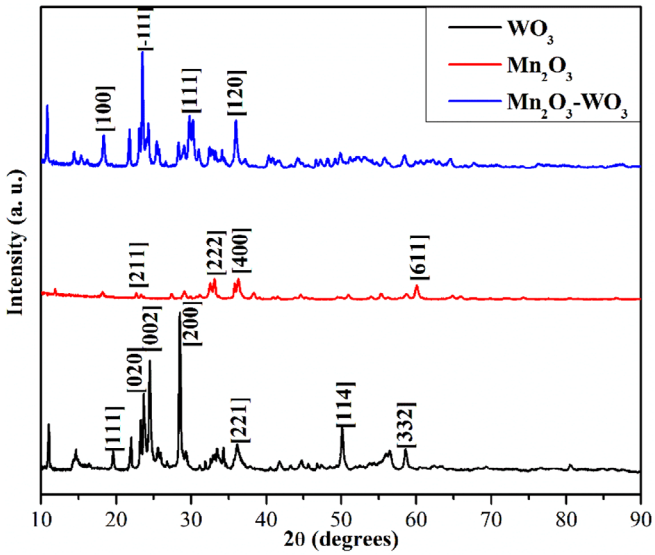

Figure 2. X-ray diffraction peaks of WO_3, Mn_2O_3, and Mn_2O_3–WO_3 photocatalyst.

does not alter the crystal structure of WO_3, indicating that the formation of the heterojunction preserves the intrinsic properties of the individual components, which are essential for photocatalytic activity.

The morphology and microstructures of the photocatalyst were examined by SEM and TEM. Figure 3 shows SEM and TEM micrographs of Mn_2O_3–WO_3 nanocomposites.

The SEM image shown in Figure 3a indicates the unique morphology of the small rod-like Mn_2O_3 nanoparticles homogeneously coalesced on the surface of WO_3, while the hierarchical structure of WO_3 is still maintained. TEM images in Figure 3b reveal the as-prepared Mn_2O_3–WO_3 nanocomposite, indicating a hierarchical structure that provides an increased effective surface area of rod-like Mn_2O_3 composite, which provides more active sites for photocatalytic reactions, while ovoid-like WO_3 aggregates scatter light more effectively. As shown in Figure 3c,d, W, O, and Mn distributions are presented by TEM EDS elemental mapping and are uniformly distributed throughout the composite. Therefore, the Mn_2O_3–WO_3 nanocomposite was successfully prepared.

3.2. Optical Properties

UV–vis diffuse reflectance spectroscopy was used to study the optical properties of WO_3 and the Mn_2O_3–WO_3 nanocomposites, as shown in Figure 4.

The UV–vis DRS and Tauc plots of the as-synthesized WO_3 and Mn_2O_3–WO_3 are shown in Figure 4a,b. Based on the results obtained, the bandgaps of WO_3 and Mn_2O_3–WO_3 are 2.43 and 1.83 eV, respectively. The narrow bandgap in the nanocomposite confirms its suitability under visible light irradiation.

Photoluminescence (PL) spectra are commonly used to determine charge separation, migration, and transfer.[34] Figure 4c shows the room-temperature photoluminescence spectra of laser-excited pure WO_3 and Mn_2O_3–WO_3 nanocomposites at 330 nm. The emission at 708 nm indicates that the Mn_2O_3–WO_3 produced is less intense than WO_3. Oxygen vacancies create a heterojunction, leading to a higher electron-hole pair separation efficiency. Several studies in the literature have indicated that oxygen vacancies improve photoactivity responses.[35–37]

3.3. BET Analysis

The N_2 absorption–desorption of WO_3 and Mn_3O_2–WO_3 was studied to indicate the increase in the specific surface area of the Mn_2O_3–WO_3 heterojunction due to the deposition of Mn_2O_3 onto the surface of WO_3, as shown in Figure 5. The isotherms of the samples in Figure 5a indicated a type IV isotherm pattern with an H3 hysteresis loop according to the IUPAC classifications.[34] The BET analyses reveal a significant increase in the specific surface area of Mn_2O_3–WO_3 (5.3033 m^2/g) composite in comparison to pristine WO_3 (3.0992 m^2/g). This increase is attributed to the deposition of Mn_2O_3 onto the WO_3 surface, which introduces additional surface roughness and porosity. The large pore volume and pore size of Mn_2O_3–WO_3 (0.807786 cm^3/g and 609.26852 nm) compared to pristine WO_3 (0.008962 cm^3/g and

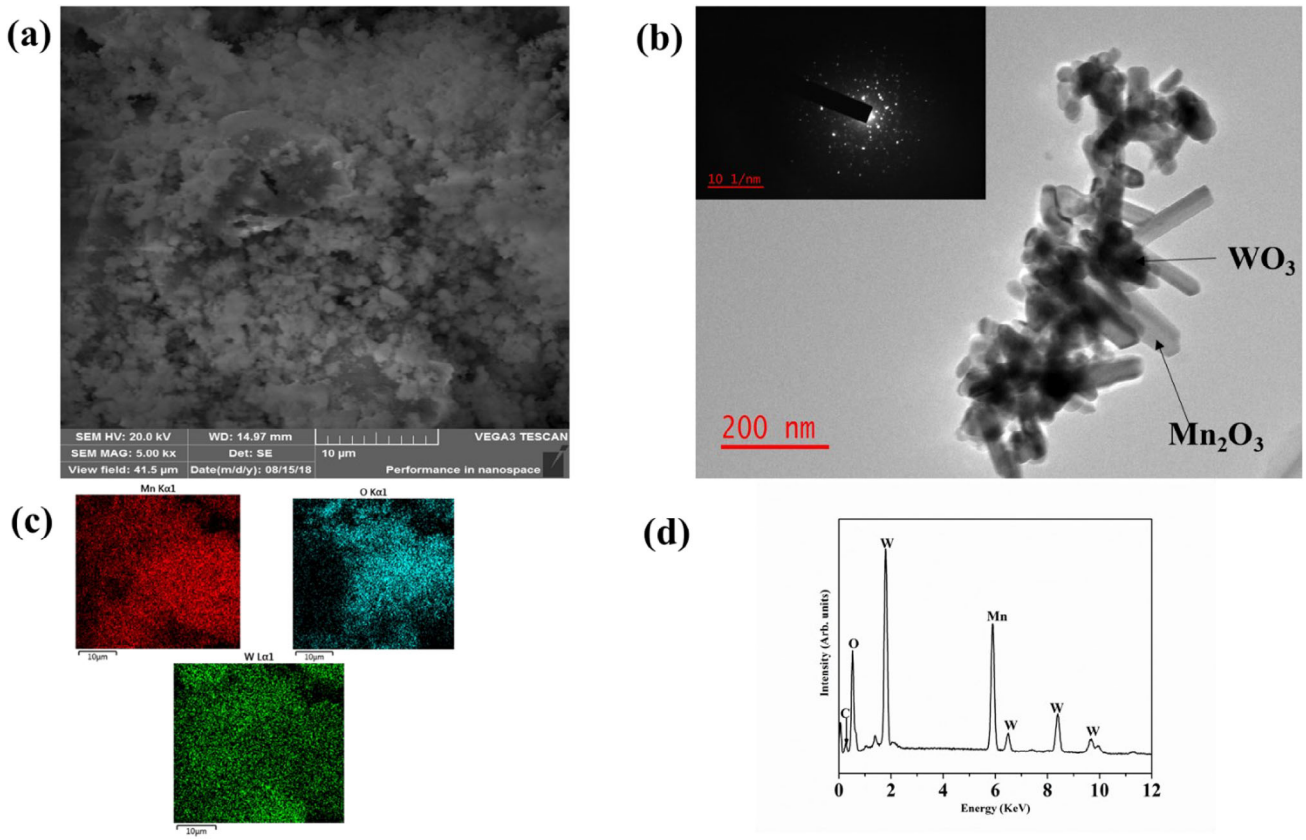

Figure 3. (a) SEM image of Mn_2O_3–WO_3, (b) TEM image of Mn_2O_3–WO_3 (inset SAED), (c) elemental mapping, and (d) EDS graph.

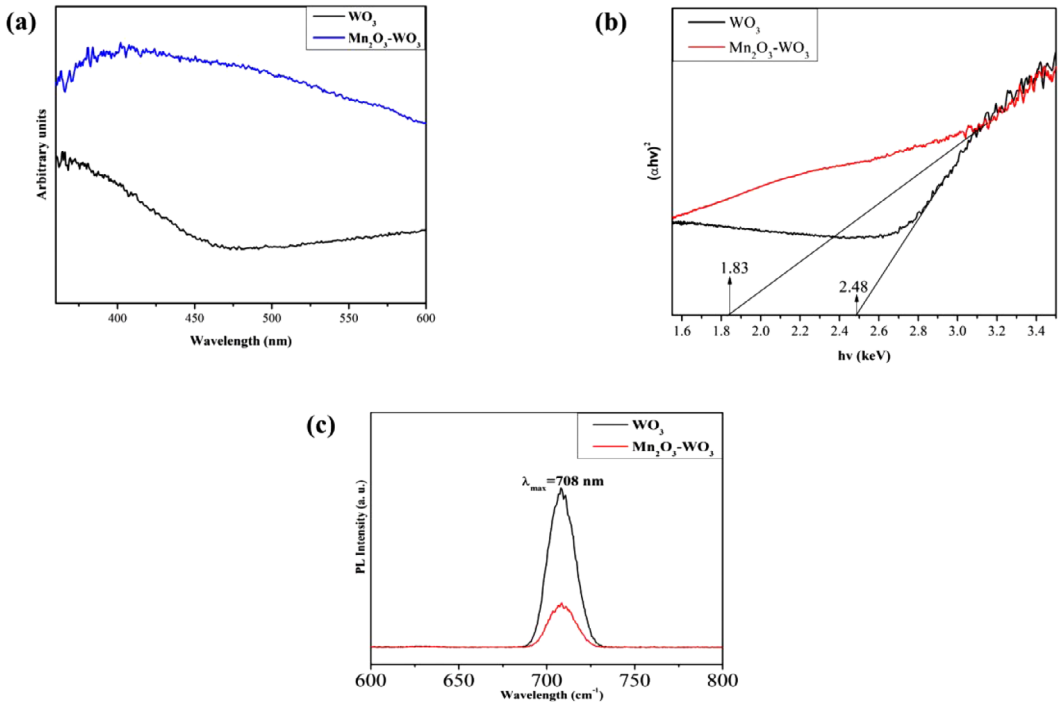

Figure 4. (a) UV–vis DRS spectra, (b) Tauc plots, and (c) PL spectra of WO_3 and Mn_2O_3–WO_3.

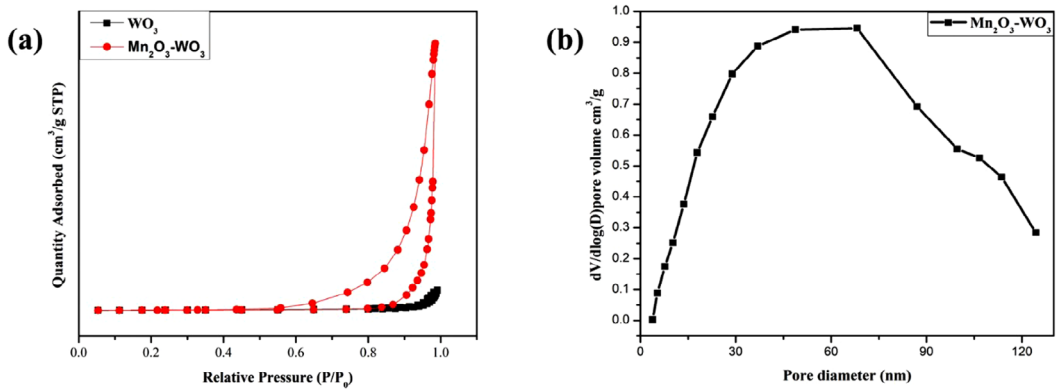

Figure 5. (a) N_2 absorption–desorption isotherms of the as-prepared WO_3 and Mn_2O_3–WO_3 nanomaterials and (b) BJH curve of the Mn_2O_3–WO_3 NPs.

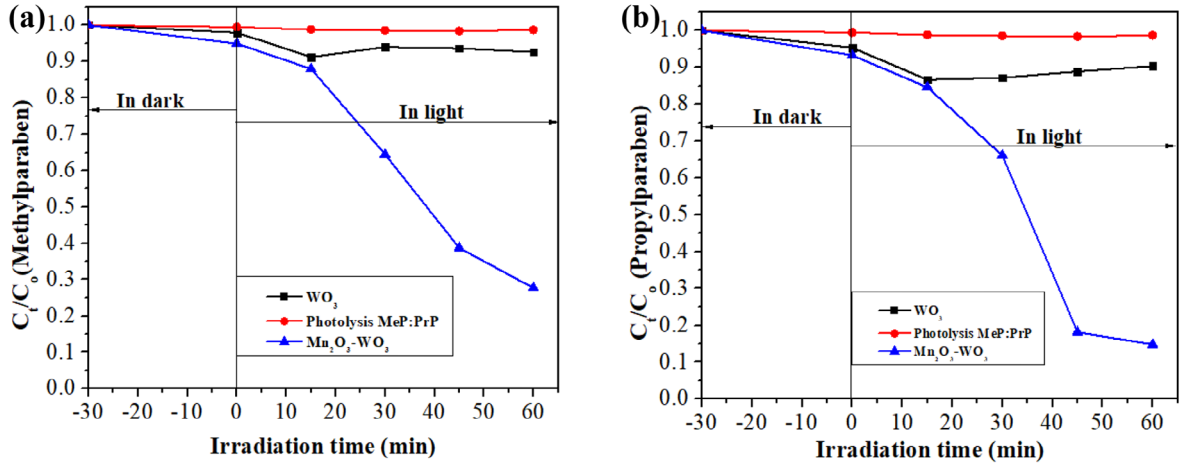

Figure 6. Photocatalytic degradation of (a) methylparaben (MeP) and (b) propylparaben (PrP) in a mixture (MeP/PrP ratio 1:3) over WO_3 and Mn_2O_3–WO_3.

11.56704 nm) further enhanced the accessibility to reactive sites for photocatalytic reactions. The BJH pore size distribution curve shown in Figure 5b shows an average 68 nm pore size for Mn_2O_3–WO_3, pointing to a mesoporous structure beneficial for photocatalytic processes.

3.4. Adsorption and Photodegradation of Mixed Parabens

The surface adsorption capabilities and photocatalytic activities of the WO_3 and Mn_2O_3–WO_3 nanocomposites for the degradation of mixed parabens were evaluated, and the results are shown in Figure 6. From the results obtained, WO_3 showed minimal decline in the degradation of mixed parabens, while Mn_2O_3–WO_3 composites showed significant improvement. The composite's high surface area and pore size provided more reaction sites for photocatalytic processes. Figure 6a,b shows that the C/C_0 values decrease with increasing time, and 60 min is the time required for the removal of mixed parabens. The composite's mesoporous structure enhanced the total light harvesting efficiency because Mn_2O_3 and WO_3 have complimentary bandgaps. Recombination loss is decreased, and the heterojunction between the two materials increases charge carrier availability. Since these compounds are more likely to be found in water and wastewater as a mixture rather than separately, the WO_3 and Mn_2O_3–WO_3 nanomaterials were tested for their ability to remove mixed pollutants from aqueous solutions. From Figure 6, the reaction appears to slow down as time increases when the mixture is utilized because the same quantity of photons is now applied to destroy a bigger load of the mixed parabens.[38] Additionally, mixed parabens had a remarkable photodegradation efficiency, hence achieving removal efficiencies of 72% and 85% for MeP and PrP, respectively. Xiao et al.[35] reported the photodegradation of mixed parabens (MeP/PrP 1:3) using $I_{0.7}$—$Bi_4O_5Br_2$ and $I_{1.0}$—$Bi_4O_5Br_2$, where the results obtained complement the results reported in this study. Furthermore, it was noted that the oxygen vacancies in MnO_x account for the final degradation efficiency.[33,36] This means that Mn_2O_3–WO_3 composites can effectively remove a mixture of parabens in water.

3.5. Reaction Mechanisms

The accumulation of electrons in WO_3's conduction band was a necessary step in the degradation of mixed parabens (methylparaben and propylparaben) by the Mn_2O_3–WO_3 heterojunction. According to the literature, the band gap of cubic bixbyite

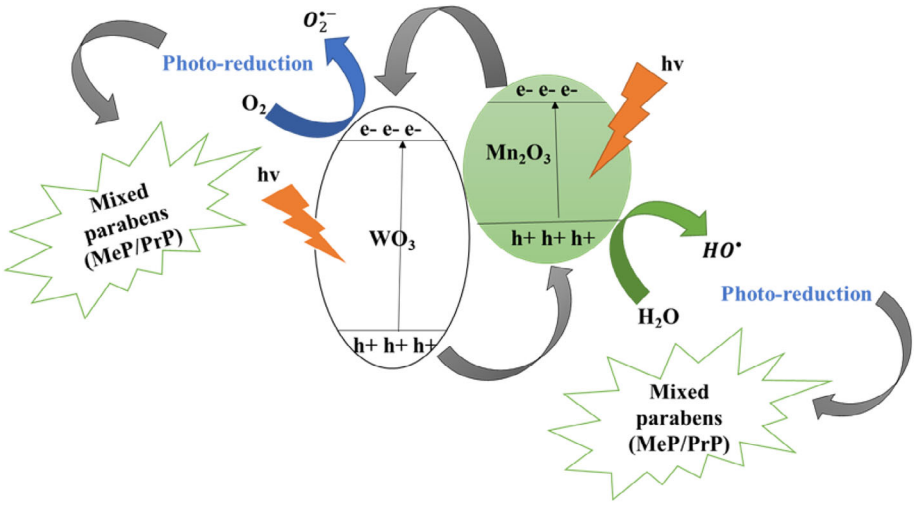

Figure 7. Schematic diagram showing the possible charge separation and transfer during the photo-oxidation process of mixed parabens under visible light.

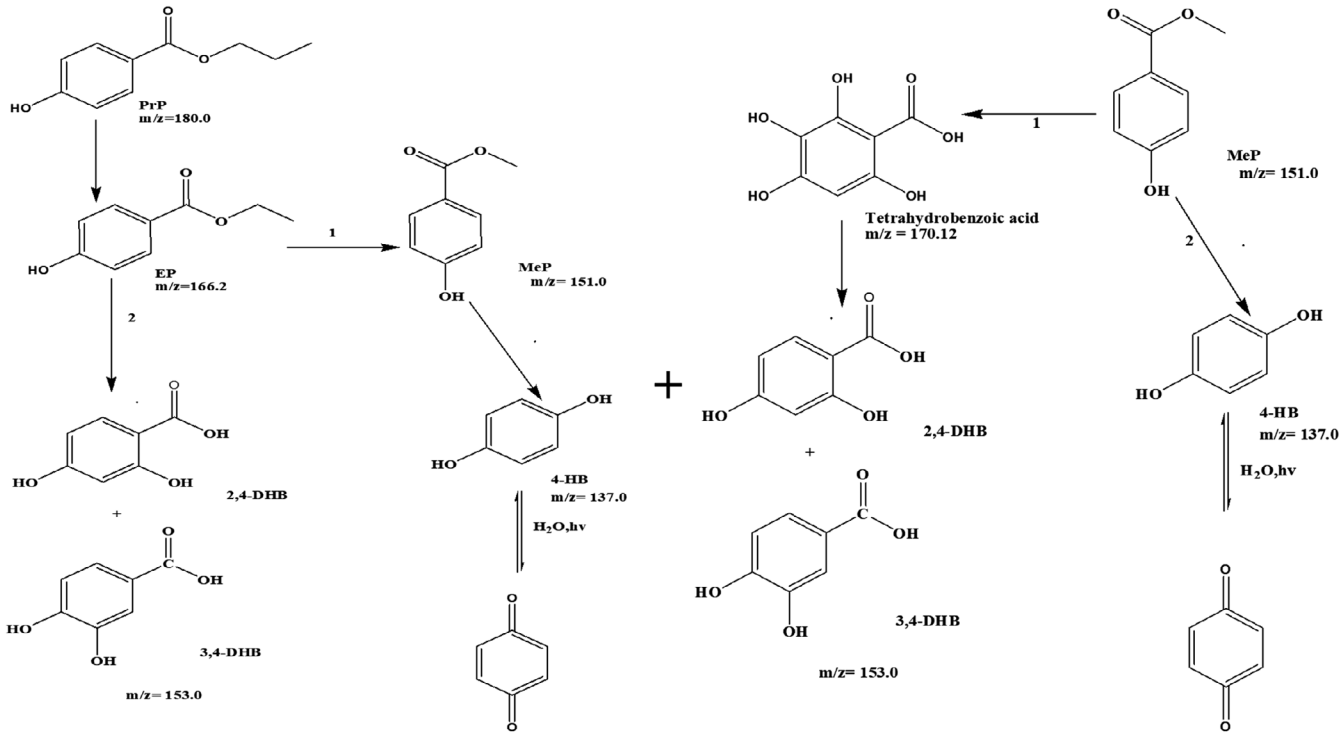

Figure 8. Degradation routes of mixed parabens and their proposed intermediates.

Mn_2O_3 ranges from 1.2 to 1.29 eV,[37] while that of WO_3 from Figure 4b is 2.48 eV. This semiconductor can produce electron/hole (e^-/h^+) pairs by absorbing visible light energy. During this process, protons and photogenerated electrons combine with superoxide ($O_2^{\bullet-}$) to make hydroxyl radicals and holes at the valence band of Mn_2O_3, where they oxidize water molecules to yield reactive hydroxyl radicals, as detailed below:

$$Mn_2O_3/WO_3 + hv \rightarrow WO_3\,(e^-) + Mn_2O_3\,(h^+)$$

$$WO_3\,(e^-) + O_2O_2^{(o-)}$$

$$WO_3\,(e^-) + O_2 \rightarrow O_2^{\bullet-}$$

$$HO_2^o + h^+ + WO_3\,(e^-)\,H_2O_2$$

$$H_2O_2 + WO_3\,(e^-) \rightarrow HO^{\bullet} + HO^-$$

$$MeP/PrP + HO^{\bullet} \rightarrow Degradationproducts$$

$$MeP/PrP\ + Mn_2O_3\,(h^+) \rightarrow Degradation\ products$$

The Mn_2O_3–WO_3 p–n heterojunction's overall remarkable performance can be explained by two observations: (i) the incorporation of Mn_2O_3, which allowed WO_3 to extend into the visible region, as stated in Figure 4a, and (ii) the formation of a p–n junction between n-type WO_3 and p-type Mn_2O_3, which helped to lower the electron-hole pair recombination at the interface, as indicated by the PL spectra results in Figure 4c. The mobility of the charge carriers to the surface, as well as the electron-hole pair recombination process, is revealed by the photoluminescence (PL) spectra analysis of the as-synthesized WO_3 and Mn_2O_3–WO_3. The intensity of PL emission is directly correlated with the recombination of excited electrons and holes. The organic contaminants MeP and PrP were able to be degraded by free electrons and holes through surface adsorption. The pathway mechanisms are schematically shown in Figure 7.

3.6. Photocatalytic Degradation Mechanism of Mixed Parabens

We carried out the irradiation experiments to characterize the photocatalytic intermediates. Five major intermediates were identified as possible degradation products. Based on identification results, tentative reaction pathways of propylparaben and methylparaben degradation in the presence of Mn_2O_3–WO_3 can be depicted in Figure 8.

As shown in Figure 8, all the intermediates are formed mainly from dealkylation, decarboxylation, and hydroxylation. Firstly, propylparaben undergoes dealkylation to form ethylparaben, which further undergoes two separate routes: route 1, dealkylation to form methylparaben, which further undergoes decarboxylation as a potential pathway to produce 1,4-dihydroxybenzene as a byproduct[38–40] or $HO^{\cdot}$ radicals attack to form 1,4-dihydroxybenzene and benzoquinone. These aromatic compound byproducts have been discussed in previous studies.[41–43] Route 2 involved a hydroxylation process whereby two isomeric byproducts were formed, namely 2,4-dihydroxybenzoic acid (2,4-DHB) and 3,4-dihydroxybenzoic acid (3,4-DHB) with the chemical formula $C_7H_5O_4^-$ (*m/z* 153.0). These intermediates have been consistently identified in multiple studies, confirming their role in the degradation process.[16,36] For the degradation pathway of methylparaben, the route 2 degradation pathway is similar to route 1 of propylparaben. For route 1, the methylparaben can undergo two possible processes: either ester hydrolysis or direct oxidation of methylparaben by oxygen dissolved in water[39] to form tetrahydrobenzoic acid (THB). The $HO^{\cdot}$ radicals are particularly effective in attacking the alkyl groups of parabens, resulting in the production of 4-hydroxybenzoic acid (4-HB) (*m/z* 137.0).[44] This highlights the role of reactive oxygen species in driving these transformations.

4. Conclusion

Pharmaceutical and personal care products (PPCPs) have been effectively eliminated using advanced oxidation methods such as electrochemical oxidation, ultrasonication, and ionizing radiation. This study has created Mn_2O_3–WO_3 nanocomposites by the sol–gel process, and they are effective photocatalysts for the removal of mixed parabens from water when exposed to visible light. Within 60 min, the nanocomposites demonstrated excellent efficiency, eliminating 72% of methylparaben and 85% of propylparaben. This study focuses on the catalyst's synthesis and initial performance; subsequent research will address reusability tests to assess its applicability on an industrial scale. Further investigations will focus on evaluating the catalyst's reusability across consecutive cycles to further assess its practical viability. The key intermediates, such as 1,4-dihydroxybenzene, 2,4-dihydroxybenzoic acid, and 3,4-dihydroxybenzoic acid, were found throughout the degradation process, mostly involving dealkylation, decarboxylation, and hydroxylation. The photocatalytic activity and visible light absorption were exhibited by Mn_2O_3–WO_3 nanocomposites, which made them a practical, affordable, and environmentally acceptable method of eliminating emerging organic pollutants like parabens from water. Therefore, this work contributes to our understanding of the photocatalytic degradation mechanisms and provides a practical approach to environmental remediation.

Acknowledgements

The authors wish to thank the Spectral Analytical Facility at the University of Johannesburg for the availability of X-ray diffraction and Transmission Electron Microscope.

Conflict of Interests

The authors declare no conflicts of interest.

Data Availability Statement

The data that support the findings of this study are available in the supplementary material of this article.

Keywords: Nanocomposites · Paraben preservatives · Photocatalysts · Sol–gel method · Visible light irradiation

[1] J. Geng, W. Fang, M. Liu, J. Yang, Z. Ma, J. Bi, *Sci. Total Environ.* **2024**, *954*, 176246.
[2] A. Wołowicz, H. M. S. Munir, *Sci. Total Environ.* **2025**, *958*, 177948.
[3] X. Li, X. Shen, W. Jiang, Y. Xi, S. Li, *Ecotoxicol. Environ. Saf.* **2024**, *278*, 116420.
[4] C. Papadopoulos, Z. Frontistis, M. Antonopoulou, D. Venieri, I. Konstantinou, D. Mantzavinos, *Ultrason. Sonochem.* **2016**, *31*, 62–70.
[5] M. G. Soni, I. G. Carabin, G. A. Burdock, *Food Chem. Toxicol.* **2005**, *43*, 985–1015.
[6] Z. Frontistis, M. Antonopoulou, D. Venieri, S. Dailianis, I. Konstantinou, D. Mantzavinos, *Catal. Today* **2017**, *280*, 139–148.
[7] X. Peng, Y. Yu, C. Tang, J. Tan, Q. Huang, Z. Wang, *Sci. Total Environ.* **2008**, *397*, 158–166.
[8] B. R. Ramaswamy, G. Shanmugam, G. Velu, B. Rengarajan, D. J. Larsson, *J. Hazard. Mater.* **2011**, *186*, 1586–1593.

[9] N. B. Bolujoko, E. I. Unuabonah, M. O. Alfred, A. Ogunlaja, O. O. Ogunlaja, M. O. Omorogie, O. D. Olukanni, *Sci. Total Environ.* **2021**, *792*, 148092.
[10] P. D. Darbre, P. W. Harvey, *J. Appl. Toxicol.* **2008**, *28*, 561–578.
[11] J. H. Tong, S. Elmore, S.-S. Huang, P. Tachachartvanich, K. Manz, K. Pennell, M. D. Wilson, A. Borowsky, M. A. La Merrill, *Endocrinology* **2023**, 164.
[12] E. Hager, J. Chen, L. Zhao, *Int. J. Environ. Res. Public Health* **2022**, *19*, 1873.
[13] S. Bai, K. Zhang, J. Sun, R. Luo, D. Li, A. Chen, *CrystEngComm* **2014**, *16*, 3289.
[14] Q. W. Cao, Y. F. Zheng, X. C. Song, *J. Taiwan Inst. Chem. Eng.* **2017**, *70*, 359–365.
[15] T. Choi, J.-S. Kim, J. H. Kim, *Adv. Powder Technol.* **2016**, *27*, 2061–2065.
[16] E. M. Ngigi, E. M. Kiarii, P. N. Nomngongo, C. J. Ngila, *ChemistrySelect* **2018**, *3*, 9845–9856.
[17] J. Zhang, H. Lu, C. Liu, C. Chen, X. Xin, *RSC Adv.* **2017**, *7*, 40499–40509.
[18] H. He, S. P. Berglund, P. Xiao, W. D. Chemelewski, Y. Zhang, C. B. Mullins, *J. Mater. Chem. A* **2013**, *1*, 12826.
[19] F. Zhan, R. Xie, W. Li, J. Li, Y. Yang, Y. Li, Q. Chen, *RSC Adv.* **2015**, *5*, 69753–69760.
[20] G.-J. Lee, A. Manivel, V. Batalova, G. Mokrousov, S. Masten, J. Wu, *Ind. Eng. Chem. Res.* **2013**, *52*, 11904–11912.
[21] R. Saravanan, V. K. Gupta, V. Narayanan, A. Stephen, *J. Taiwan Inst. Chem. Eng.* **2014**, *45*, 1910–1917.
[22] P. Li, C. Nan, Z. Wei, J. Lu, Q. Peng, Y. Li, *Chem. Mater.* **2010**, *22*, 4232–4236.
[23] T. D. Schladt, K. Koll, S. Prüfer, H. Bauer, F. Natalio, O. Dumele, R. Raidoo, S. Weber, U. Wolfrum, L. M. Schreiber, M. P. Radsak, H. Schild, W. Tremel, *J. Mater. Chem.* **2012**, *22*, 9253.
[24] M. Y. Nassar, A. S. Amin, I. S. Ahmed, S. Abdallah, *J. Taiwan Inst. Chem. Eng.* **2016**, *64*, 79–88.
[25] Y. Shao, B. Ren, H. Jiang, B. Zhou, L. Lv, J. Ren, L. Dong, J. Li, Z. Liu, *J. Hazard. Mater.* **2017**, *333*, 222–231.
[26] A. Berenjian, L. Maleknia, G. Chizari Fard, A. Almasian, *J. Taiwan Inst. Chem. Eng.* **2018**, *86*, 57–72.
[27] Y. Wang, J. Cui, L. Luo, J. Zhang, Y. Wang, Y. Qin, Y. Zhang, X. Shu, J. Lv, Y. Wu, *Appl. Surf. Sci.* **2017**, *423*, 1182–1187.
[28] L. Chen, Y. Liu, L. Yang, C. Xu, W. Wang, G. Li, Y. Zhu, M. Zhou, Z. Hou, *Chem. Eng. Sci.* **2024**, *285*, 119626.
[29] A. V. Radhamani, M. Krishna Surendra, M. S. Ramachandra Rao, *Mater. Des.* **2018**, *139*, 162–171.
[30] A. Umar, I. Jung, A. A. Ibrahim, M. S. Akhtar, S. A. Kumar, M. A. M. Alhamami, T. Almas, N. Almehbad, S. Baskoutas, *J. Energy Storage* **2024**, *81*, 110305.
[31] M. Shanmugaprabu, K. Kanthavel, *Phys. B* **2022**, *647*, 414282.
[32] T. Choi, J.-S. Kim, J. H. Kim, *Adv. Powder Technol.* **2016**, *27*, 347–353.
[33] X. Yu, M. Shi, Y. Fan, L. Yang, J. Zhang, W. Liu, W. Dai, S. Zhang, L. Zhou, X. Luo, S. Luo, *Appl. Catal., B* **2022**, *309*, 121236.
[34] K. S. Sing, *Pure Appl. Chem.* **1982**, *54*, 2201–2218.
[35] X. Xiao, M. Lu, J. Nan, X. Zuo, W. Zhang, S. Liu, S. Wang, *Appl. Catal., B* **2017**, *218*, 398–408.
[36] A. Baral, D. P. Das, M. Minakshi, M. K. Ghosh, D. K. Padhi, *ChemistrySelect* **2016**, *1*, 4277–4285.
[37] A. S. Ryabova, S. Y. Istomin, K. A. Dosaev, A. Bonnefont, J. Hadermann, N. A. Arkharova, A. S. Orekhov, R. P. Sena, V. A. Saveleva, G. Kéranguéven, E. V. Antipov, E. R. Savinova, G. A. Tsirlina, *Electrochim. Acta* **2021**, *367*, 137378.
[38] M. Gmurek, A. F. Rossi, R. C. Martins, R. M. Quinta-Ferreira, S. Ledakowicz, *Chem. Eng. J.* **2015**, *276*, 303–314.
[39] M. Cifre-Herrando, G. Roselló-Márquez, D. García-García, J. Garcia-Anton, *Nanomaterials* **2022**, *12*, 4286.
[40] S. A. Khan, M. Jain, K. K. Pant, Z. M. Ziora, M. A. Blaskovich, *Ind. Eng. Chem. Res.* **2023**, *62*, 6646–6659.
[41] Y. Lin, C. Ferronato, N. Deng, F. Wu, J.-M. Chovelon, *Appl. Catal., B* **2009**, *88*, 32–41.
[42] K.-i. Okamoto, Y. Yamamoto, H. Tanaka, M. Tanaka, A. Itaya, *Bull. Chem. Soc. Jpn.* **1985**, *58*, 2015–2022.
[43] V. Augugliaro, L. Palmisano, A. Sclafani, C. Minero, E. Pelizzetti, *Toxicol. Environ. Chem.* **1988**, *16*, 89–109.
[44] A. Petala, Z. Frontistis, M. Antonopoulou, I. Konstantinou, D. I. Kondarides, D. Mantzavinos, *Water Res.* **2015**, *81*, 157–166.

Manuscript received: March 3, 2025